Supplemental Material for: Scanning X-ray diffraction microscopy for diamond quantum sensing

Mason C. Marshall,[1,2,3] David F. Phillips,[2] Matthew J. Turner,[3,4,5] Mark J.H. Ku,[3,6,7] Tao Zhou,[8] Nazar Delegan,[9,10] F. Joseph Heremans,[9,10,11] Martin V. Holt,[8] and Ronald L. Walsworth[1,2,3,12]

[1] *Department of Electrical Engineering and Computer Science, University of Maryland, College Park, Maryland, 20742, USA*
[2] *Center for Astrophysics | Harvard & Smithsonian, Cambridge, Massachusetts, 02138, USA*
[3] *Quantum Technology Center, University of Maryland, College Park, Maryland, 20742, USA*
[4] *Department of Physics, Harvard University, Cambridge, Massachusetts, 02138, USA*
[5] *Center for Brain Science, Harvard University, Cambridge, Massachusetts, 02138, USA*
[6] *Department of Physics and Astronomy, University of Delaware, Newark, Delaware, 19716, USA*
[7] *Department of Materials Science and Engineering, University of Delaware, Newark, Delaware, 19716, USA*
[8] *Center for Nanoscale Materials, Argonne National Laboratory, Lemont, Illinois, 60439, USA*
[9] *Center for Molecular Engineering, Argonne National Laboratory, Lemont, Illinois, 60439, USA*
[10] *Materials Science Division, Argonne National Laboratory, Lemont, Illinois, 60439, USA*
[11] *Pritzker School of Molecular Engineering, University of Chicago, Chicago, Illinois, 60439, 60637, USA*
[12] *Department of Physics, University of Maryland, College Park, Maryland, 20742, USA*

(Dated: Draft: October 15, 2021)

I. SUPPLEMENTAL MATERIAL

A. Sample information

The CVD quantum sensing diamond used in this study was produced by Element Six, inc. It features a 40 μm thick overgrowth layer, grown via (001) chemical vapor deposition atop an electronic-grade, single-crystal substrate, with less than 5 ppb of both N and NV. Before growth, the substrate was mechanically polished. The overgrowth layer was grown with isotopically purified carbon, with 99.95% ^{12}C, and doped with 10 parts per million (ppm) of ^{15}N. After growth, the diamond was electron-irradiated and annealed to form NV centers in the N-doped layer. The resulting NV^- density is approximately 1 ppm, similar to sister samples used in previous work [1, 2].

We note that the electron irradiation also helps to resolve concerns about charge- and dipole-trapping near damage tracks affecting QDM measurements. In high-NV-density diamonds, which have been irradiated with a high fluence of electrons, a single additional charge will have little to no effect on the electric-field environment. (However, note that this electron irradiation cannot initiate nuclear recoil chains which would interfere with damage track detection - conservation of momentum dictates each electron will create only one or a few lattice site vacancies.) Said electron irradiation also does not tend to form large numbers of permanent dipoles, as evidenced by the lack of strong electric-field signals in NV spectroscopy on irradiated diamonds. This may be a result of diamond's semiconductor nature; electron-hole pairs, once induced, will either recombine or drift through the lattice to charge-trapping impurities, rather than form enduring dipoles near the damage track [3–5]. The same should be true for ionization induced by WIMP- or particle-induced damage tracks. (Additionally, see Sec. I M below for a discussion of potential electric-field contributions to QDM measurements.)

We additionally note that the isotopic purification is significant for many diamond quantum sensing applications, as removal of ^{13}C nuclear spins enhances quantum defect coherence times and reduces transition linewidths [6]. However, the isotopic makeup of the diamond has little effect on the SXDM measurements; and for QDM measurements such as those reported here, isotopic purification is relevant only when the strain-induced frequency shifts to be sensed are small enough to be comparable in magnitude with the linewidth reduction from isotopic purification.

The HPHT diamond featured in main text Fig. 2 was produced by Element Six, inc, using type Ib high-pressure, high-temperature synthesis. Produced using carbon with natural isotopic abundance together with approximately 100-200 ppm of nitrogen, this HPHT diamond features more homogeneous overall strain than the layered CVD sample, but lacks the dense NV ensemble required for magnetic or strain imaging using NV spin-state spectroscopy. The HPHT diamond surface contains imperfections or defects, which were identified prior to SXDM scanning via confocal laser microscopy; main text Fig. 2 shows an SXDM scan of one group of these features. The exact nature of these features is not known, but could include surface imperfections due to microscopic polishing damage; clusters of pointlike defects; or surface contamination from photolithographic processing and metallization of fiducial markers. Independent of the feature origin, however, the physical scale of the features is comparable to the 100-nm scale expected for WIMP- or particle-induced damage tracks.

B. Constraining contributions from changes in lattice orientation

In this work, crystal lattice strain is measured via shifts in the X-ray Bragg diffraction pattern. Similar shifts in the diffraction pattern may also result from changes of orientation in the crystal lattice. However, while strain-induced changes in lattice spacing of the diffracting crystal planes can only shift the diffraction pattern along the detector 2θ axis, a changing lattice orientation can shift the diffraction pattern along either detector axis. Characterizing the position of the diffraction pattern along the detector X axis can thus help constrain the contribution of lattice orientation changes to the observed diffraction pattern shifts. We characterize such shifts by finding the edges of the central low-count region induced by the beam stop [7], shown in Fig. 1a. We find that the average vertical positions in the strain features and the overall diffraction profile are equal, as shown in Fig. 1b. This disfavors changes in lattice orientation as the main source of the observed diffraction pattern shifts, except for orientations that coincidentally yield little or no X position shift.

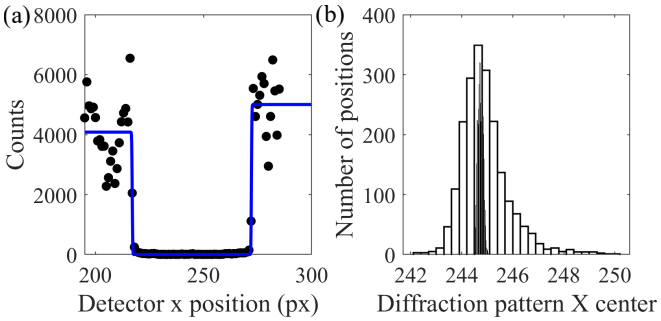


FIG. 1. **(a)** Representative diffraction pattern summed over the 2θ axis, together with a fit to an error function used to determine the center of the diffraction pattern along the X axis. **(b)** Histograms of such "X centers" for the overall diffraction pattern (black bars) and reduced diffraction pattern (white bars), for X-ray beam positions intersecting growth defect feature A (as labeled in Fig. 4 of the main text). The white histogram is broader because of the comparatively fewer photons contributing to the reduced lineshape. The equal centers of these distributions favor compressive strain as the likely origin of the diffraction pattern shifts, as discussed in the text.

Comparison of the measurements performed using (113) and ($\bar{1}$13) diffraction enable us to further constrain possible contributions from changes in lattice orientation. Features A and C of Fig. 5 of the main text exhibit a centroid shift in the reduced diffraction curve lineshape by an amount consistent with equal strain along both projections. We also observe vertical diffraction pattern shifts of one pixel or less in both projections. This constrains the possible directions of lattice orientation in these strain features to only those that yield nearly zero vertical diffraction shift for both Bragg conditions, as well as a horizontal shift consistent with equal strain. While such orientation changes cannot be ruled out by our measurements, strain with Burgers vector in the $\langle 110 \rangle$ family of crystal axes is a more plausible explanation, since it both explains the observations and is known to be a dominant class of growth defects in diamond [8]. This contributes to our choice in Sec. II of the main text to present results in the uniform-orientation scenario. More generally, while some of the shifts in the diffraction pattern may be caused by orientation changes as well as strain, in this work we demonstrate a sensitivity to strain sufficient, e.g., to detect WIMP dark matter signals.

C. Constructing local host-crystal diffraction profiles

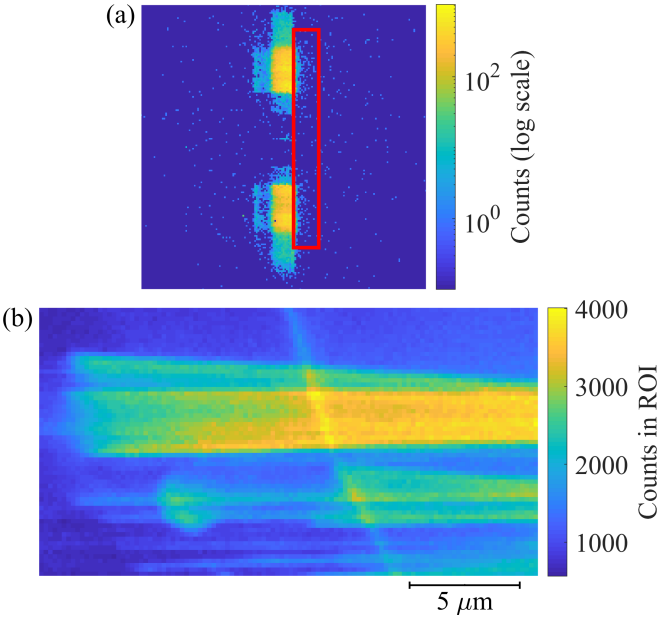


FIG. 2. **(a)** Example region of interest (ROI) for initial analysis to classify X-ray beam positions as "strained" or "host crystal;" the detector ROI for identifying local strain features is marked by the red box. **(b)** Total counts in the detector ROI for each beam position within a subset of the region scanned in main text Fig. 5.

In order to calculate the reduced diffraction pattern used for analysis of short-length strain features, we first construct local host-crystal diffraction profiles. This requires an initial classification of each X-ray beam position as "strained" or "host crystal" depending on whether the beam intersects a strain feature. We base this initial classification on a "region of interest" (ROI) analysis, where we define detector regions that count photons scattered by compressively strained regions of the diamond. Figure 2a shows such an ROI on an example diffraction pattern, while Fig. 2b shows a map of total counts in this ROI for all beam positions in one spatial scan. Beam

positions with more than a threshold number of counts in this ROI are identified as "strained," while positions with less than this threshold are identified as interacting only with the host crystal. To determine the appropriate threshold, we measure the distribution of counts in a region of "pristine" diamond without strain features; the threshold is chosen to be approximately two standard deviations of this distribution above the mode of count numbers in each column of a spatial scan, to account for spatial intensity gradients such as that visible in Fig. 2b. We check this thresholding procedure by manually defining "strain" and "host crystal" regions for several spatial scans; the results show good agreement. We note that this initial classification is used only to generate the host-crystal profile; in the final analysis, each beam position is re-classified based on parameters of the reduced diffraction pattern fit. The overall analysis procedure is therefore robust to occasional initial misclassifications of specific beam positions.

As can be seen in Fig. 2b, this ROI analysis reveals a smooth horizontal gradient in intensity across the field of view, likely originating from variation in the separation between sample and focusing optics as the X-ray beam is rastered across the sample. We therefore construct a separate local host-crystal diffraction profile for each column of a spatial scan by averaging all diffraction patterns from "unstrained" beam positions within that column. Dividing by the local host-crystal diffraction profile thus suppresses the inhomogeneous signal from the unstrained diamond, while simultaneously removing the effect of these horizontal gradients. This procedure yields reduced diffraction patterns such as the one featured in Fig. 4b of the main text.

D. Calibration curves

To convert between the position of the diffraction peak on the detector and the strain in the short-length-scale crystal feature, we use a calibration curve. To generate this curve, we use the kinematic approximation for crystal diffraction [9, 10] to simulate diffraction patterns for an unstrained diamond substrate with and without an additional thin strained layer, representing the strain feature. The results of one such simulation are presented in Fig. 3a. We then take the ratio between the two diffraction curves, replicating the process by which we generate the reduced diffraction patterns (as discussed in Sec. II of the main text). This gives a simulated reduced diffraction curve which can be fit to extract its centroid, as shown in Fig. 3b. Finally, this process is repeated for different strain values in the layer, generating a calibration curve, as shown in Fig. 3c.

Each point in Fig. 3a-b represents a column of detector pixels. In the real detector, these pixels count diffracted X-ray photons integrated over a finite area rather than a single point. To replicate this in our calibration and avoid possible aliasing effects, we initially oversample the simulated diffraction curve by a factor of 12; we then sum the oversampled calibration curves into bins representing the physical detector pixels.

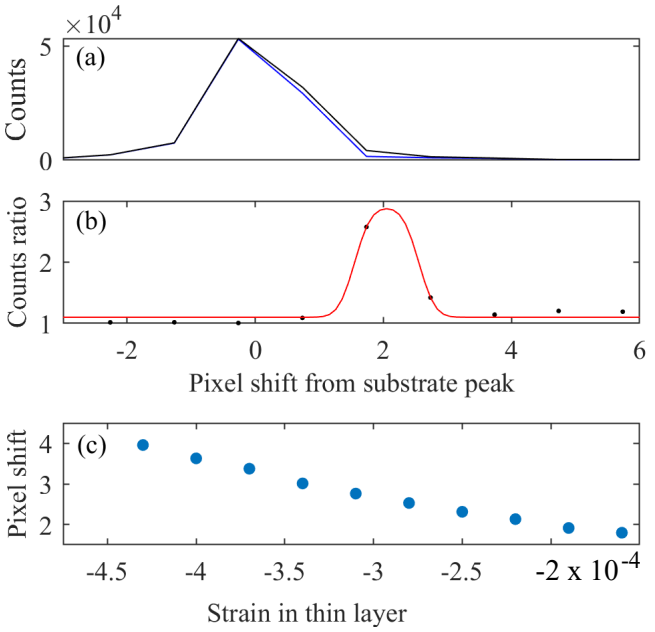


FIG. 3. Steps for generation of calibration curves to allow conversion between the X-ray diffraction peak position and and short-length-scale strain feature. **(a)** A diffraction curve is simulated for an unstrained substrate with (black) and without (blue) a thin layer of strained crystal. **(b)** Dividing these two curves gives a simulated reduced diffraction curve; this is fit to obtain its centroid. **(c)** This is repeated for different strain values to obtain a calibration curve.

In order to test the robustness of this calibration and characterize its uncertainty, we generated calibration curves while varying several parameters in the kinematic diffraction simulation. These include the thickness of the strained layer; the linewidth of the diffraction peak due to the unstrained substrate; the amplitude of diffraction peaks from the substrate and strained layer; the amount of oversampling performed; and the position of bin edges when summing the oversampled points. Amplitude and oversampling parameters are found not to significantly affect the calibration; uncertainty in the calibration due to strain feature thickness and unstrained diffraction peak linewidth are discussed in supplemental material Sec. I F.

E. Identifying strain feature edges via vertical asymmetry

One additional limitation of the lineshape analysis and calibration procedure relates to strain feature thickness: at positions where the X-ray beam intersects the strained feature for less than ∼200 nm, the calibration is less reliable. The Bragg diffraction peak width from a layer

increases as the layer thickness decreases; for very thin layers, some portion of the diffraction peak may overlap with the large, slowly varying diffraction profile and be suppressed by the empirical lineshape reduction.

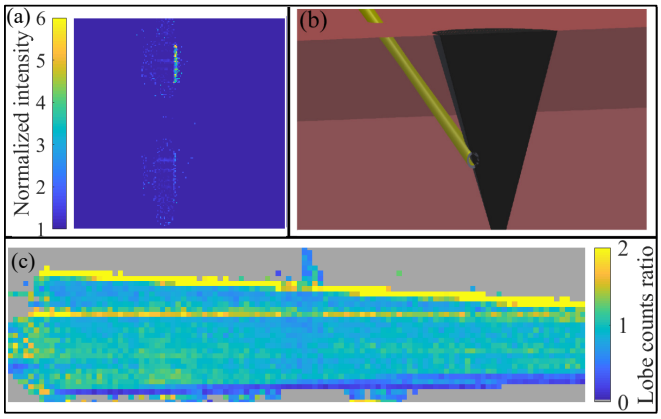


FIG. 4. Identifying region edges and narrow features using X-ray diffraction-pattern asymmetry. **(a)** Reduced lineshape analysis as described in Sec. 2 of the main text, performed on a beam position at the edge of a strained volume. X-rays are diffracted into the feature peak for only half of the annular beam. **(b)** Schematic model of X-ray interactions at edge. Away from the focal plane, the beam spot size grows; at the sharp edge of a feature, only one-half of the annulus intersects the feature and diffracts X-rays to the detector. **(c)** Map of the top-bottom asymmetry of feature peaks, for one "petal" feature in the (113) projection shown in main text Fig. 5. High or low asymmetry values signal the beam is at the edge of a feature.

To avoid miscalibrated measurements, we identify the edges of growth defects, where the intersection with the beam may be problematically short. We perform this identification by examining the two-dimensional shape of the reduced diffraction pattern. The diffraction pattern is divided into two "lobes", separated by a low-count region created by the central beam stop of the focusing optic [7] (as is visible in Fig. 4a-b of the main text). At the sharp edges of a growth defect, we see different diffraction from the two lobes, implying significant strain variation over the tens of nanometers of the beam spot. Away from the sharp edges, X-rays in each lobe diffract identically, as the separation between lobes is miniscule compared to the length scale of strain features. Diffraction patterns from the sharp edges of strain features thus show asymmetry between the two lobes, which is emphasized in the reduced diffraction pattern. Figure 4a shows a reduced diffraction pattern for such an edge, with the upper lobe having significantly more intensity after the lineshape reduction. Figure 4b shows a schematic example of a beam spot at the edge of a growth defect, with only one half of the beam intersecting the strained diamond, creating such a pattern.

To quantify this asymmetry, we extract the ratio of counts in the upper and lower lobes for each reduced diffraction pattern. Fig. 5 shows the distribution of this ratio for beam positions in the region of Fig. 5 of the main text. If this ratio is less than 0.5 or greater than 2, we classify that beam position as an "edge", with additional uncertainty in the calibration between diffraction curve centroid and strain due to the short distance of interaction between the beam and the strained layer. All such "edge" pixels identified in main text Fig. 5 and supplemental material Fig. 6 feature high measured strain; the color bar upper limit thus represents a lower bound on the strain present in the defect features. When the layer is thicker than $\sim$ 200 nm, this calibration uncertainty is limited to 1.5E-5, as presented in table I.

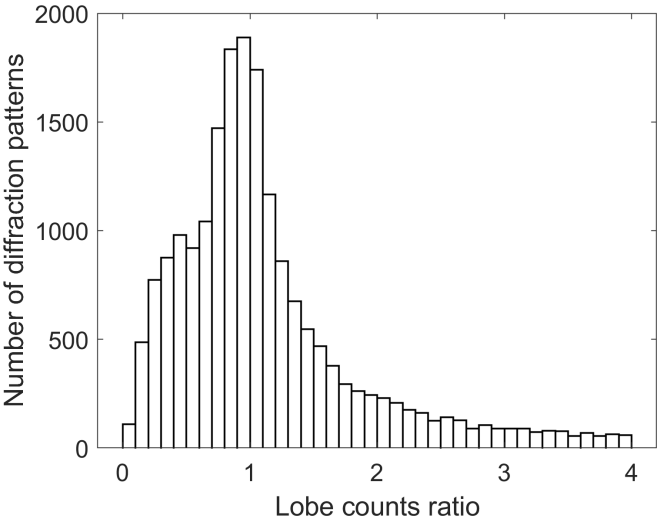


FIG. 5. Histogram of counts ratios for all X-ray beam positions featured in Fig. 4 of the main text. We label all features with count ratio less than 0.5 or greater than 2 as "edge" points.

F. Uncertainty in strain measurements

Sec. II of the main text describes the process of extracting quantitative strain values from SXDM diffraction patterns recorded on the detector. The most significant systematic uncertainties enter through the calibration curves. Table I presents the leading uncertainties for a typical measurement of a strain feature.

TABLE I. Error budget for a typical SXDM strain feature measurement using methods described in this study.

Error Source	Uncertainty
Statistical	2.0E-5
Feature thickness	1.5E-5
Unstrained peak linewidth	1.2E-5
Dynamical diffraction effects	0.9E-5
Total	2.9E-5

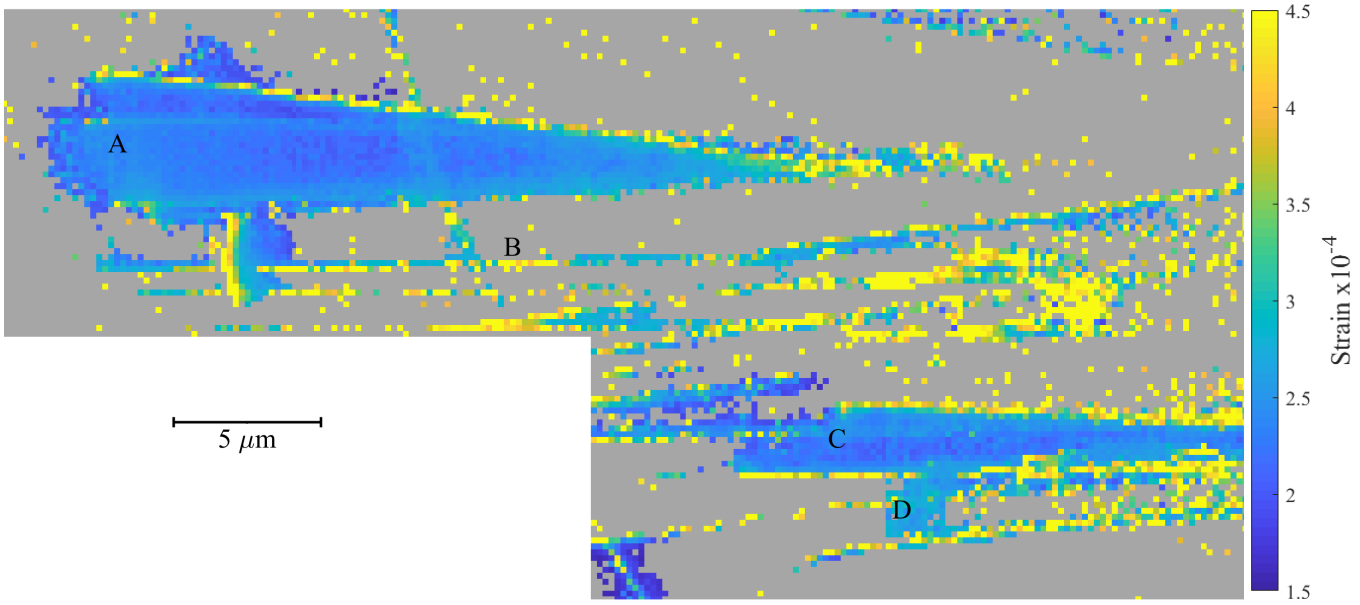


FIG. 6. SXDM strain map of the region featured in main text Fig. 5, as measured with $(\bar{1}13)$ diffraction using a 200 nm scan step size. The data was analyzed using the same background subtraction method detailed in main text Sec. II.

The thinner a strain feature is, the wider that feature's diffraction peak. Whatever part of the diffraction peak overlaps the large host-crystal diffraction peak will be suppressed when we divide to emphasize sharply varying features; the wider the true diffraction peak is, the more this suppression will shift the centroid of the reduced peak. The calibration curve therefore shows some dependence on the thickness of the strained layer, especially for very thin strain features. However, as discussed in Sec. I E, beam positions that only briefly interact with the edges of strain features can be distinguished by the two-dimensional distribution of counts on the detector. After removing such positions from our analysis, the remaining effect of feature thickness on the strain calibration is reflected in our error budget above.

Similarly, the linewidth of the unstrained diffraction pattern enters into the denominator of the empirical lineshape reduction analysis. The error budget reflects the range of host-crystal peak widths measured in this work.

Finally, our calibration curves are constructed using the kinematic approximation for diffraction pattern construction, while a more complete analysis would include dynamical diffraction effects. To evaluate the potential distortion due to this approximation, we benchmark our kinematic approximation calculations by comparison to publicly available dynamical diffraction code [11, 12] for the (004) mirror plane, and include the maximum observed difference as a conservative estimate of the resulting uncertainty.

G. Strain map for $(\bar{1}13)$ diffraction

Figure 6 shows a strain map measured with $(\bar{1}13)$ diffraction on the same region of the CVD quantum sensing diamond as featured in Fig. 5 of the main text. Strain values are extracted using the same analysis procedure described in main text Sec. II, except with calibration curves generated for this diffraction condition. Note that "petal" features A and C appear in both projections with equal strain (within the measurement uncertainty), while feature B and most of feature D are absent; this is likely due to different average Burgers vectors between features, as discussed in the main text. As with main text Fig. 5, this scan used a step size of 200 nm, and the color scale is chosen to allow the reader to see the internal strain variation within the "petals."

H. Diffraction curves without background subtraction

Figure 7 shows a log-scale plot of diffraction curves before the background subtraction analysis for the same four beam positions presented in Fig. 3c of the main text, together with the corresponding local host-crystal diffraction profiles. The ratio of measured diffraction curve to local host-crystal profile gives the reduced diffraction curves of Fig. 3c of the main text. The minimum detectable strain shift of $\sim$ 1.5 detector pixels originates from the linewidth of the host-crystal diffraction profile; diffraction signals from features with less than this strain are suppressed in the generation of reduced diffraction

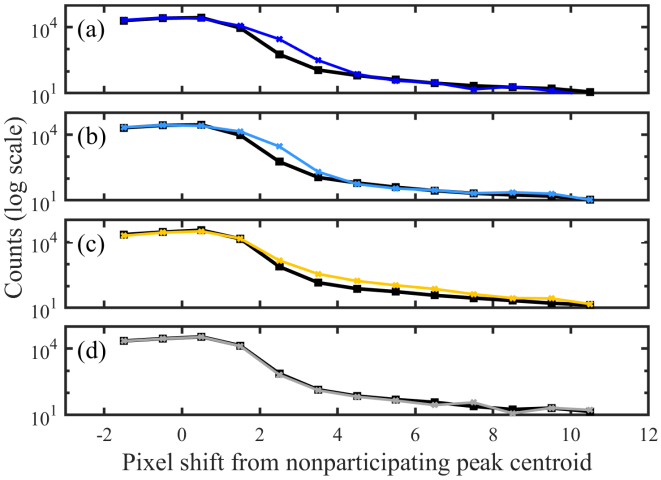


FIG. 7. Log-scale plot of SXDM diffraction curves without the empirical lineshape analysis (for the same beam positions featured in Fig. 2 of the main text and with the same colors), together with the corresponding local host-crystal diffraction profiles (black points).

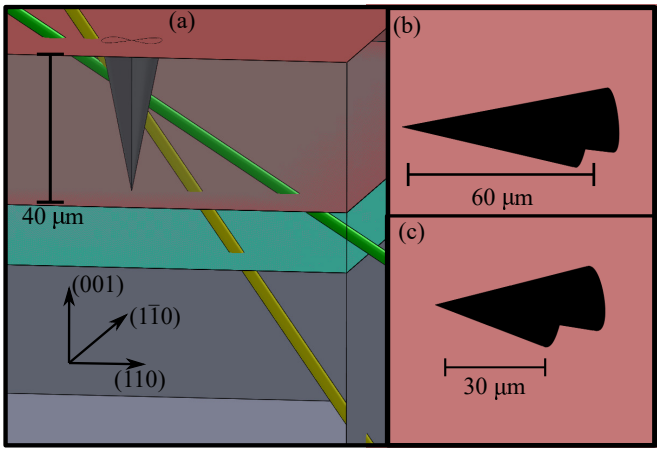


FIG. 8. Schematic of diamond interrogation with HXN. This figure demonstrates the interrogation of a two-leaf "clover" feature, nucleating at the CVD-substrate interface and propagating along the growth direction, similar to those observed in this study. As in Fig. 1 of the main text, the green beam addresses the (113) crystal plane, while the yellow beam addresses ($\bar{1}$13). Panel **(b)** shows the two-dimensional projection observed by the (113) beam, while **(c)** shows the ($\bar{1}$13) projection.

curves.

I. Illustration of three-dimensional "petal" feature projected onto two-dimensional data

As discussed in the main text, the largest strain structures observed in this study take the form of "petal"-shaped growth defect regions, which nucleate at the substrate-CVD interface and propagate upwards. Only two lobes of each feature are observed here, as opposed to the four lobes in similar features observed in [1], because of the different detection thresholds for compressive and tensile strain discussed in Sec. II of the main text. Fig. 8 shows a schematic illustration of two-dimensional projection of such features by the X-ray beam, which creates (for example) the data patterns of Fig. 5 of the main text.

J. "Petal" and "rod" strain features

We construct a three-dimensional geometrical model of strain features from two feature types, referred to as "petals" and "rods." "Petal" features include conical volumes with a droplet-shaped cross-section and a shared core, nucleating at or near the substrate-layer interface and growing upwards close to the CVD growth direction. "Rod" features are thin cylinders which also nucleate at or near the substrate-layer interface, but which may branch out as they grow.

Defects with these shapes have been identified in past studies of strain features in CVD diamond. "Petal" defects have been observed experimentally [1, 13] and modeled theoretically [14]. This modelling has shown that they comprise bundles of many individual dislocations which together create the observed strain fields. Meanwhile, "rod" dislocations could represent either the high-strain edges of otherwise unmeasured "petals", or single or bundled linear dislocations. X-ray tomography identified "rod"-like features as both edge and mixed dislocations in bundles of different densities [8] (albeit with insufficient spatial resolution to differentiate "petal" features). In both cases, these features propagated at a variety of angles to the growth direction. TEM studies of single dislocations in CVD diamond [15] have shown that they alternate between screw and edge segments with different propagation directions, giving an average propagation at an angle to the growth axis.

We use observed "petal" and "rod" features as examples of three-dimensional strained volumes that affect NV sensing, and with which we can demonstrate the capabilities of SXDM. The observed "petal" features have internal strain similar to that expected near a particle-induced crystal damage track; measuring their structure serves as a demonstration of the three-dimensional capability of stereoscopic SXDM over tens of microns of depth, as well as a benchmark of strain sensitivity. While the measurements presented in main text Fig. 5 and supplemental material Fig. 6 do not allow conclusive determination of the structure of the "petals," they do reveal certain interesting features about these structures – especially the increasing strain at their edges. This may indicate that the density of individual dislocations is higher towards the edges or at the outer surface of the volume.

We note that past X-ray tomography [8] has distinguished edge from mixed dislocations in "rod"-like strain

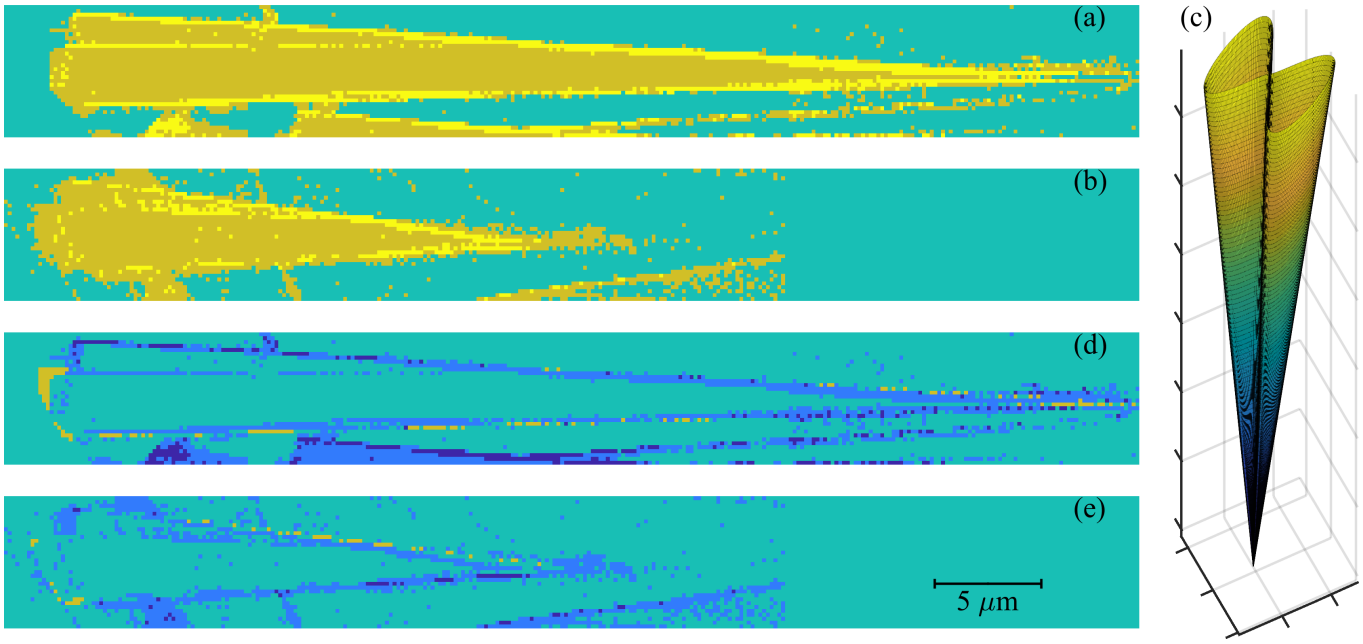


FIG. 9. Constraining 3-D strain geometric model parameters with SXDM data. **(a)-(b)**: Classified data for the upper conical strain feature from the (113) (upper) and ($\bar{1}$13) (lower) projections. Each beam position is classified based on feature peak fits as either host crystal (teal), strained subvolume (orange), or edge (yellow). **(c)**: A three-dimensional model is constructed, which can be projected onto the two measurement planes. **(d)-(e)**: Residuals after subtracting each data set from the appropriate model projection. The sum of squared differences can be fed into a minimizing algorithm to optimize geometric parameters of the model.

features based on their Burgers vector. However, to create a high-fidelity three-dimensional model we only analyzed "rods" which appear in both (113) and ($\bar{1}$13) projections, leaving their Burgers vectors ambiguous. We also note that the local strain fields of screw, edge, and mixed dislocations fall off with different powers of distance from the dislocation core; however, to efficiently map the entire volume around features A, B, C, and D, we opted for a scan step size of 200 nm, which gives insufficient spatial resolution to perform such an analysis.

K. Lack of "small" strain features in main text Fig. 5

We note the lack of observed strain features ∼1 micron or smaller in main text Fig. 5 for the CVD diamond, in comparison to those mapped in the HPHT diamond and shown in main text Fig. 2. This result is in part due to the larger scan step size used in main text Fig. 5, which would have caused some of the features in main text Fig. 2 to appear as single pixels, if at all. We note that strain features ∼ 100 nm in at least one dimension are observed when a smaller scan step size is used on this diamond, as seen in main text Fig. 10b.

Aspects of the manufacturing and history of the CVD diamond also likely reduce the prevalence of small features. For example, the surface of the NV-enriched overgrowth layer was not mechanically polished after growth, meaning there are no small strain features associated with microscopic mechanical surface. (While the substrate-overgrowth interface was polished, microscopic defects there would propagate through the overgrowth layer; this is in fact a likely origin for features like A, B, C, and D, as discussed below.) Additionally, the CVD diamond was high-temperature annealed after electron irradiation to create NV centers. This likely dissociated or alleviated strain due to vacancies and vacancy clusters incorporated during CVD growth and irradiation, as discussed in main text Sec. V.

L. Constraining geometrical parameters of the three-dimensional model

To create a geometric model of strained volumes in the CVD diamond, we first identify "petal" and "rod" features. "Petal" features are identified by conical shapes containing strained diamond, as features A, B, C, and D in main text Fig. 5. "Rod" features are identified as thin linear high-strain features propagating through the overgrowth layer. To avoid unconstrained features and overfitting, we only identify "rod" features that are at least partially present in both (113) and ($\bar{1}$13) projections. For each identified feature, we then construct a surface in parametric coordinates. For "petals," we

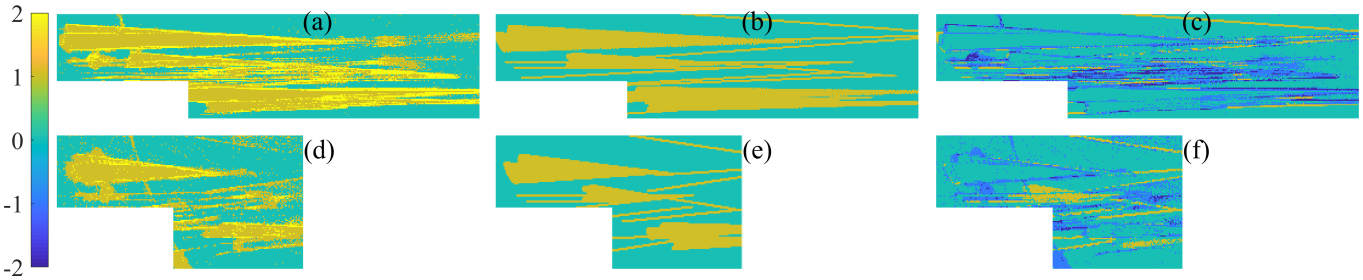


FIG. 10. Full comparison of strain geometric model with SXDM data. **(a)**: Data from the (113) projection, classified in the same way as the example in Fig. 9. **(b)**: Projection of the geometrical model onto the (113) diffraction plane. **(c)**: Residuals after subtracting data from projection. **(d)-(f)**: Same as above but for the ($\bar{1}$13) projection.

start with paired conical surfaces with drop-shaped cross-section, defined with respect to parametric coordinates (R, Θ):

$$\begin{aligned} X &= R\left(\sin\left(\pm\phi_1\right)\cos\left(\Theta\right)\right) \\ Y &= R\left(a\sin\left(\Theta\right)\right)\sin\left(\frac{\Theta}{2}\right)^{l} \\ Z &= R. \end{aligned} \tag{1}$$

We rotate each surface by $\pm\theta_1$ about the Y-axis, leaving the tips of the drop-shaped cross-sections touching at the shared core of the "petal." We then rotate the entire shape by angles ϕ_2 and ϕ_3 around the X and Z axes, respectively. Fig. 9c shows a model "petal" constructed in this way. The free parameters for the shape are thus a and ϕ_1, which determine the two elliptical axes of the cross-section; l, which determines the steepness of the drop profile; and ϕ_2 and ϕ_3, which determine the overall spatial orientation of the feature; as well as the origin (x,y,z) near the CVD-substrate interface. We construct "rods" similarly, with a circle of radius a replacing the drop-shaped cross-section, and with additional rods branching off along the length of the original rod. After constructing the volumes, we project each entity onto surfaces at angles corresponding to the (113) and ($\bar{1}$13) Bragg diffraction conditions. Finally, we compare these projections to categorized SXDM data giving the positions of strain features, and constrain the geometrical free parameters by minimizing residuals of this comparison.

Fig. 9 gives an example of the optimization procedure for determining the parameters of a single "petal" feature. Fig. 9a-b show the categorized data used for this comparison. We classify each point as either only intersecting the host crystal, part of the strained subvolume, or an edge of the strained subvolume, based on the amplitude of the reduced diffraction curve (see Fig. 3 of the main text) and the vertical asymmetry in the diffraction pattern (see supplemental material Sec. I E). Fig. 9c shows the initial three-dimensional model for a "petal" feature. (Only two of the four lobes of the "petal" are present because we only observe the compressively strained parts of the feature, while the diffraction signal from the tensile-strained lobes is concealed by the large host-crystal diffraction profile from the substrate - see Sec. II of the main text for details.) Fig. 9d-e show the comparison between SXDM strain data and the model. To calculate residuals, we assign a value of 2 to each pixel classified as an "edge" and 1 to each classified as part of the strained subvolume; we subtract pixel-by-pixel to obtain the difference maps in Fig. 9d-e. To obtain a quantity that can be minimized, we sum the absolute value of all pixels in the difference maps. Minimizing these residuals gives the position, shape, size, and angle of the feature for the three-dimensional strain feature model of Fig. 6 of the main text. Figure 10 shows the classified data, projected model, and subtracted residuals for both Bragg conditions.

M. Overview of strain measurement methods using a quantum diamond microscope (QDM)

The quantum diamond microscope (QDM) measurements presented in the main text use nitrogen vacancy (NV) center spin-state spectroscopy for strain imaging of diamond on micron to millimeter scales. The methods and apparatus used for these QDM measurements are presented in detail in Ref. [1]; in this section we give a brief overview.

The NV center comprises a substitutional nitrogen impurity adjacent to a vacancy in the carbon lattice. The NV axis can lie along the four $\langle 111\rangle$ crystallographic axes; Figure 11a sketches the crystal structure for these four possible classes of NV centers. Collectively, the NV forms a spin-1 electronic system, with a simplified schematic of the NV spin and electronic energy level structure given in Fig. 11b. The spin energy levels in the electronic ground state are sensitive to environmental parameters, including both electromagnetic fields [16–20] and strain [1, 21, 22]. In the presence of a bias magnetic field $|\vec{B}| > 1$ mT (as used in this work), the NV ground-state spin Hamiltonian reduces to [1]

$$H_\kappa = (D + M_{z,\kappa})S_{z,\kappa}^2 + \gamma\vec{B}\cdot\vec{S}_{z,\kappa}, \tag{2}$$

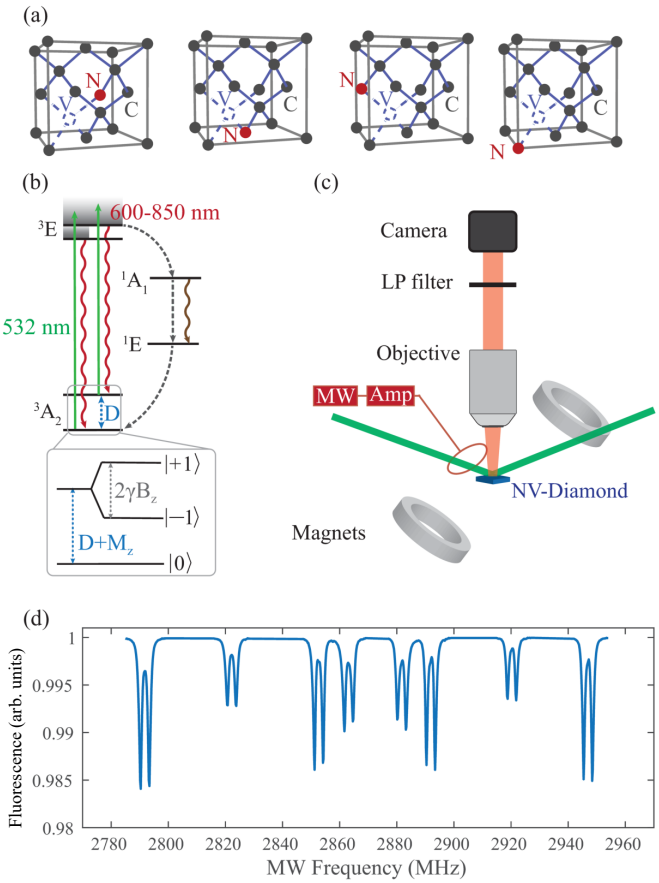


FIG. 11. Overview of strain imaging with a quantum diamond microscope (QDM). **(a)** Crystal structure of the NV center, demonstrating the four possible NV crystallographic axes. **(b)** Simplified NV energy level structure. Inset shows ground state spin energy levels. See text for details. **(b)** Schematic of QDM apparatus. NVs are excited by green laser light, while red fluorescence is collected by a microscope objective and imaged onto a camera. A magnetic bias field is provided by permanent magnets, and microwaves are applied using a loop antenna. **(d)** Example NV spin spectrum measured by a QDM (see text for details).

where $\kappa = (1, 2, 3, 4)$ represents the four possible crystallographic orientations of the NV axis within the crystal lattice, $D \approx 2870$ MHz is the temperature-dependent zero-field splitting, M_z is the energy level shift induced by stress along the axis between nitrogen and vacancy (defined to be the z axis in the NV coordinate system), and S_z is the spin-1 projection operator along that axis. Spectroscopic measurements of the spin transition frequencies under this Hamiltonian form the basis of QDM measurements.

NV centers have several attractive properties for quantum sensing. Specifically, the electronic structure enables both optical initialization and readout of the spin state, allowing fast and accurate microwave spectroscopy of the spin transition frequencies. In a typical NV measurement, green laser light excites the electronic state into a phonon sideband; the excited state usually decays via spin-state-conserving spontaneous emission of red fluorescence. A second decay path through a pair of singlet states exhibits increased coupling to the $|m_s = \pm 1\rangle$ states over $|m_s = 0\rangle$, and does not emit into the same wavelength band. NV centers in the $|m_s = 0\rangle$ state therefore exhibit enhanced fluorescence, allowing optical spin-state readout. Further, the alternative decay path does not conserve the spin state, meaning repeated excitation with green fluorescence gives nearly complete spin polarization into $|m_s = 0\rangle$.

A QDM performs microwave spectroscopy of the ground-state spin transitions using this optical initialization and readout. A schematic of a typical QDM apparatus is shown in Fig. 11c: green laser light excites the NV centers for optical initialization and readout, while red fluorescence is collected by a microscope objective and imaged onto a camera. Permanent magnets provide a bias magnetic field, and microwaves broadcasted to the NVs by a loop antenna drive spin transitions when resonant. For NV strain imaging, the microwave drive frequency is swept across the resonance profile, and the red fluorescence collected at each frequency step. When the microwaves are off-resonant, the laser polarizes the NV spins into $|m_s = 0\rangle$, maximizing the collected fluorescence. However, when the microwaves are resonant they drive transitions into either the $|m_s = +1\rangle$ or $|m_s = -1\rangle$ state with enhanced coupling to the alternative decay path, reducing the fluorescence.

Figure 11d shows an example spectrum acquired in this fashion. The eight visible resonances correspond to the $|m_s = 0\rangle \rightarrow |m_s = +1\rangle$ and $|m_s = 0\rangle \rightarrow |m_s = -1\rangle$ transition frequencies for each of the four NV classes, which are typically equally populated in a CVD-grown ensemble diamond. The two narrower lines within each resonance represent hyperfine transitions with the spin-1/2 ^{15}N nucleus. In this measurement, the magnetic field direction was chosen to have a different projection along each of the four NV axes, giving different values of $\gamma\vec{B} \cdot \vec{S}_{z,\kappa}$ and therefore different spin transition frequencies. The spectrum can be simultaneously fit to equation (2) to extract $M_{z,\kappa}$ for all four NV axes. Measuring both the $|m_s = +1\rangle$ and $|m_s = -1\rangle$ transitions allows separation of the stress and magnetic field contributions to the Hamiltonian, as the stress term is proportional to S_z^2 and therefore shifts both transitions in the same direction, while the magnetic field term is proportional to S_z and therefore shifts the $|m_s = +1\rangle$ and $|m_s = -1\rangle$ transitions in opposite directions.

To create a strain image such as those presented in the main text of this work, a camera acquires spatially resolved images of red fluorescence at each frequency point of the microwave sweep; this yields a spectrum such as that shown in Fig. 11d for each camera pixel. Fitting each of these spectra to equation (2) determines all four $M_{z,\kappa}$ values at each pixel of the image. Finally, the proper linear combination of the four $M_{z,\kappa}$ values gives the stress

tensor elements, which can be converted to strain via the measured elasticity tensor of diamond [23] (as mentioned in the main text). For details of the conversion between $M_{z,\kappa}$ and stress tensor, see Ref. [1].

To complement the earlier discussion of charge- and dipole-trapping near damage tracks, we briefly note that while electric fields and strain couple through the same operators in an inseparable way for individual NV centers, in an ensemble of NV centers the effects can be distinguished, because stress is a tensor whereas electric field is a vector quantity. For each of the four NV classes within the ensemble, the NV axis points along a different crystallographic direction; within each of these classes, there are two possible orientations between the nitrogen and vacancy (N-V and V-N, so to speak). While NVs pointing along both of these directions see the same stress-induced frequency shift $M_{z,\kappa}$, an electric field will shift their resonance frequencies in opposite directions. Large electric fields will therefore split each of the eight resonances into two sub-resonances, while small electric fields may broaden the resonance linewidths; but electric fields cannot contribute the resonance frequency shifts from which $M_{z,\kappa}$ is determined.

[1] P. Kehayias, M. J. Turner, R. Trubko, J. M. Schloss, C. A. Hart, M. Wesson, D. R. Glenn, and R. L. Walsworth, Imaging crystal stress in diamond using ensembles of nitrogen-vacancy centers, Physical Review B **100**, 174103 (2019).

[2] M. J. Turner, N. Langellier, R. Bainbridge, D. Walters, S. Meesala, T. M. Babinec, P. Kehayias, A. Yacoby, E. Hu, M. Lončar, R. L. Walsworth, and E. V. Levine, Magnetic field fingerprinting of integrated-circuit activity with a quantum diamond microscope, Physical Review Applied **14**, 014097 (2020).

[3] H. Pernegger, S. Roe, P. Weilhammer, V. Eremin, H. Frais-Kölbl, E. Griesmayer, H. Kagan, S. Schnetzer, R. Stone, W. Trischuk, D. Twitchen, and A. Whitehead, Charge-carrier properties in synthetic single-crystal diamond measured with the transient-current technique, Journal of Applied Physics **97**, 073704 (2005).

[4] M. Gabrysch, E. Marklund, J. Hajdu, D. J. Twitchen, J. Rudati, A. M. Lindenberg, C. Caleman, R. W. Falcone, T. Tschentscher, K. Moffat, P. H. Bucksbaum, J. Als-Nielsen, A. J. Nelson, D. P. Siddons, P. J. Emma, P. Krejcik, H. Schlarb, J. Arthur, S. Brennan, J. Hastings, and J. Isberg, Formation of secondary electron cascades in single-crystalline plasma-deposited diamond upon exposure to femtosecond x-ray pulses, Journal of Applied Physics **103**, 064909 (2008).

[5] H. Jayakumar, J. Henshaw, S. Dhomkar, D. Pagliero, A. Laraoui, N. B. Manson, R. Albu, M. W. Doherty, and C. A. Meriles, Optical patterning of trapped charge in nitrogen-doped diamond, Nature Communications **7**, 12660 (2016).

[6] G. Balasubramanian, P. Neumann, D. Twitchen, M. Markham, R. Kolesov, N. Mizuochi, J. Isoya, J. Achard, J. Beck, J. Tissler, V. Jacques, P. R. Hemmer, F. Jelezko, and J. Wrachtrup, Ultralong spin coherence time in isotopically engineered diamond, Nature Materials **8**, 383–387 (2009).

[7] M. Holt, R. Harder, R. Winarski, and V. Rose, Nanoscale hard x-ray microscopy methods for materials studies, Annual Review of Materials Research **43**, 183–211 (2013).

[8] M. P. Gaukroger, P. M. Martineau, M. J. Crowder, I. Friel, S. D. Williams, and D. J. Twitchen, X-ray topography studies of dislocations in single crystal cvd diamond, Diamond and Related Materials **17**, 262–269 (2008).

[9] J. A. Tilka, J. Park, Y. Ahn, A. Pateras, K. C. Sampson, D. E. Savage, J. R. Prance, C. B. Simmons, S. N. Coppersmith, M. A. Eriksson, M. G. Lagally, M. V. Holt, and P. G. Evans, Combining experiment and optical simulation in coherent x-ray nanobeam characterization of si/sige semiconductor heterostructures, Journal of Applied Physics **120**, 015304 (2016).

[10] A. Ying, B. Osting, I. C. Noyan, C. E. Murray, M. Holt, and J. Maser, Modeling of kinematic diffraction from a thin silicon film illuminated by a coherent, focused x-ray nanobeam, Journal of Applied Crystallography **43**, 587–595 (2010).

[11] A. Pateras, J. Park, Y. Ahn, J. A. Tilka, M. V. Holt, H. Kim, L. J. Mawst, and P. G. Evans, Dynamical scattering in coherent hard x-ray nanobeam bragg diffraction, Physical Review B **97**, 235414 (2018).

[12] K. Gardner, E. Mueller, J. Tilka, and P. Evans, X-ray nanobeam dynamical diffraction simulator, `https://xray.engr.wisc.edu/nanobeamsimulation/dynamicalhtml/index.php`, accessed: 2020-09-09.

[13] A. Crisci, F. Baillet, M. Mermoux, G. Bogdan, M. Nesládek, and K. Haenen, Residual strain around grown-in defects in cvd diamond single crystals: A 2d and 3d raman imaging study, physica status solidi (a) **208**, 2038–2044 (2011).

[14] H. Pinto and R. Jones, Theory of the birefringence due to dislocations in single crystal cvd diamond, Journal of Physics: Condensed Matter **21**, 364220 (2009).

[15] N. Tsubouchi and Y. Mokuno, Configuration of a single grown-in dislocation corresponding to one etch pit formed on the surface of cvd homoepitaxial diamond, Journal of Crystal Growth **455**, 71–75 (2016).

[16] E. V. Levine, M. J. Turner, P. Kehayias, C. A. Hart, N. Langellier, R. Trubko, D. R. Glenn, R. R. Fu, and R. L. Walsworth, Principles and techniques of the quantum diamond microscope, Nanophotonics **8**, 1945–1973 (2019).

[17] R. Schirhagl, K. Chang, M. Loretz, and C. L. Degen, Nitrogen-vacancy centers in diamond: Nanoscale sensors for physics and biology, Annual Review of Physical Chemistry **65**, 83–105 (2014).

[18] A. Boretti, L. Rosa, J. Blackledge, and S. Castelletto, Nitrogen-vacancy centers in diamond for nanoscale magnetic resonance imaging applications, Beilstein Journal of Nanotechnology **10**, 2128–2151 (2019).

[19] J. M. Taylor, P. Cappellaro, L. Childress, L. Jiang, D. Budker, P. R. Hemmer, A. Yacoby, R. Walsworth,

and M. D. Lukin, High-sensitivity diamond magnetometer with nanoscale resolution, Nature Physics **4**, 810–816 (2008).

[20] G. Balasubramanian, I. Y. Chan, R. Kolesov, M. Al-Hmoud, J. Tisler, C. Shin, C. Kim, A. Wojcik, P. R. Hemmer, A. Krueger, T. Hanke, A. Leitenstorfer, R. Bratschitsch, F. Jelezko, and J. Wrachtrup, Nanoscale imaging magnetometry with diamond spins under ambient conditions, Nature **455**, 648–651 (2008).

[21] D. Broadway, B. Johnson, M. Barson, S. Lillie, N. Dontschuk, D. McCloskey, A. Tsai, T. Teraji, D. Simpson, A. Stacey, J. McCallum, J. Bradby, M. Doherty, L. Hollenberg, and J.-P. Tetienne, Microscopic imaging of the stress tensor in diamond using in situ quantum sensors, Nano Letters **19**, 4543–4550 (2019).

[22] M. E. Trusheim and D. Englund, Wide-field strain imaging with preferentially aligned nitrogen-vacancy centers in polycrystalline diamond, New Journal of Physics **18**, 123023 (2016).

[23] C. A. Klein and G. F. Cardinale, Young's modulus and poisson's ratio of cvd diamond, in *Diamond Optics V*, Vol. 1759 (International Society for Optics and Photonics, 1992) p. 178–193.